

# Constraining new physics from Higgs measurements with Lilith: update to LHC Run 2 results

Sabine Kraml<sup>1\*</sup>, Tran Quang Loc<sup>2</sup>, Dao Thi Nhung<sup>2</sup>, Le Duc Ninh<sup>2</sup>

<sup>1</sup> Laboratoire de Physique Subatomique et de Cosmologie, Université Grenoble-Alpes, CNRS/IN2P3, 53 Avenue des Martyrs, F-38026 Grenoble, France

<sup>2</sup> Institute For Interdisciplinary Research in Science and Education, ICISE, 590000, Quy Nhon, Vietnam

\* sabine.kraml@lpsc.in2p3.fr

July 26, 2019

## Abstract

Lilith is public python library for constraining new physics from Higgs signal strength measurements. We here present version 2.0 of Lilith together with an updated database which includes the full set of ATLAS and CMS Run 2 Higgs results for  $36 \text{ fb}^{-1}$ . Both the code and the XML database where extended from the ordinary Gaussian approximation employed in Lilith-1.1 to using variable Gaussian and Poisson distributions. Moreover, Lilith can now make use of correlation matrices of arbitrary dimension. We provide detailed validations of the implemented experimental results as well as a status of global fits for *i)* reduced Higgs couplings and *ii)* Two-Higgs-doublet models of Type-I and Type-II. Lilith-2.0 is available on GitHub and ready to be used to constrain a wide class of new physics scenarios.

## Introduction

Introduce Higgs couplings fits and Lilith [1] .....

.....

.....

.....

.....

.....

.....

## Extended XML format for experimental input

In the *Lilith* database, every single experimental result is stored in a separate XML file. This allows to easily select the results to use in a fit, and it also makes maintaining and updating the database rather easy.

The root tag of each XML file is `<expmu>`, which has two mandatory attributes, `dim` and `type` to specify the type of signal strength result. Production and decay modes are specified via `prod` and `decay` attributes either directly in the `<expmu>` tag or as efficiencies in `<eff>` tags. Additional (optional) information can be provided in `<experiment>`, `<source>`, `<sqrts>`, `<CL>` and `<mass>` tags. Taking the  $H \rightarrow \gamma\gamma$  result from the combined ATLAS and CMS Run 1 analysis [2] as a concrete example, the structure of the XML file is

```
<expmu decay="gammagamma" dim="2" type="n">
  <experiment>ATLAS-CMS</experiment>
  <source type="publication">CMS-HIG-15-002; ATLAS-HIGG-2015-07</source>
  <sqrts>7+8</sqrts>
  <mass>125.09</mass>
  <CL>68%</CL>

  <eff axis="x" prod="ggH">1.</eff>
  <eff axis="y" prod="VVH">1.</eff>

  <!-- (...) -->
</expmu>
```

where `<!-- (...) -->` is a placeholder for the actual likelihood information. For a detailed description, we refer to the original *Lilith* manual [1]. In the following, we assume that the reader is familiar with the basic syntax.

So far, the likelihood information could be specified in one or two dimensions in the form of [1]: 1D intervals given as best fit with  $1\sigma$  error; 2D likelihood contours described as best fit point and parameters  $a, b, c$  which parametrize the inverse of the covariance matrix; or full likelihood information as 1D or 2D grids of  $-2\log L$ . The first two options, 1D intervals and 2D likelihood contours, declared as `type="n"` in the `<expmu>` tag, employ an ordinary Gaussian approximation; in the 1D case, asymmetric errors are accounted for by putting together two one-sided Gaussians with the same mean but different variances, while the 2D case assumes symmetric errors. This does not always allow to describe the experimental data (i.e. the true likelihood) very well. Full 2D likelihood grids would be much better but are rarely available.

In order to treat asymmetric uncertainties in a better way, we have extended the XML format and fitting procedure in *Lilith* to Gaussian distributions of variable width (“variable Gaussian”) as well as generalized Poisson distributions. The declaration is `type="vn"` for variable Gaussian or `type="p"` for Poisson distribution in the `<expmu>` tag. Both work for 1D and 2D data with the same syntax. Moreover, in order to make use of the  $N$ -dimensional ( $N > 2$ ) correlation matrices which both ATLAS and CMS have started to provide, we have added a new XML format for correlated signal strengths in more than two dimensions. This can be used with the ordinary or variable Gaussian approximation for the likelihood. In the following we give explicit examples for the different possibilities.

## 1D likelihood parameterization

For 1D data, the format remains the same as in [1]. For example, a signal strength  $\mu(ZH, b\bar{b}) = 1.12^{+0.50}_{-0.45}$  is implemented as

```
<bestfit>1.12</bestfit>
<param>
  <uncertainty side="left">-0.45</uncertainty>
  <uncertainty side="right">0.50</uncertainty>
</param>
```

The `<bestfit>` tag contains the best-fit value, while the `<uncertainty>` tag contains the left (negative) and right (positive)  $1\sigma$  errors.<sup>1</sup> The choice of likelihood function is done by setting `type="n"` for ordinary, 2-sided Gaussian (as in `Lilith-1.1`); `type="vn"` for a variable Gaussian; or `type="p"` for a Poisson distribution in the `<expmu>` tag.

## 2D likelihood parameterization

For `type="vn"` and `type="p"`, signal strengths in 2D with a correlation are now described in an analogous way as 1D data. For example,  $\mu(\text{ggH}, WW) = 1.10^{+0.21}_{-0.20}$  and  $\mu(\text{VBF}, WW) = 0.62^{+0.36}_{-0.35}$  with a correlation of  $\rho = -0.08$  can be implemented as

```
<expmu decay="WW" dim="2" type="vn">
  <eff axis="x" prod="ggH">1.0</eff>
  <eff axis="y" prod="VBF">1.0</eff>
  <bestfit>
    <x>1.10</x>
    <y>0.62</y>
  </bestfit>
  <param>
    <uncertainty axis="x" side="left">-0.20</uncertainty>
    <uncertainty axis="x" side="right">+0.21</uncertainty>
    <uncertainty axis="y" side="left">-0.35</uncertainty>
    <uncertainty axis="y" side="right">+0.36</uncertainty>
    <correlation>-0.08</correlation>
  </param>
</expmu>
```

Here, the `<eff>` tag is used to declare the `x` and `y` axes. The `<bestfit>` tag specifies the location of the best-fit point in the `(x,y)` plane. The `<uncertainty>` tags contain the left (negative) and right (positive)  $1\sigma$  errors for the `x` and `y` axes, and finally the `<correlation>` tag specifies the correlation between `x` and `y`. The choice of likelihood function is again done by setting `type="vn"` or `type="p"` in the `<expmu>` tag.

To ensure backwards compatibility, `type="n"` however still requires the tags `<a>`, `<b>`, `<c>` to give the inverse of the covariance matrix instead of `<uncertainty>` and `<correlation>`, see [1].

<sup>1</sup>The values in the `<uncertainty>` tag can be given with or without a sign.

## 117 Multi-dimensional data

118 For correlated signal strengths in more than 2 dimensions, a new format is introduced.  
 119 We here illustrate it by means of the CMS result [3], which has signal strengths for 24  
 120 production and decay mode combinations plus a  $24 \times 24$  correlation matrix. First, we set  
 121 `dim="24"` and label the various signal strengths as axes `d1`, `d2`, `d3`, ... `d24`:<sup>2</sup>

```
122 <expmu dim="24" type="vn">
123   <eff axis="d1" prod="ggH" decay="gammagamma">1.0</eff>
124   <eff axis="d2" prod="ggH" decay="ZZ">1.0</eff>
125   <eff axis="d3" prod="ggH" decay="WW">1.0</eff>
126   ...
127   <eff axis="d24" prod="ttH" decay="tautau">1.0</eff>
```

128 The best-fit values for each axis are specified as

```
129   <bestfit>
130     <d1>1.16</d1>
131     <d2>1.22</d2>
132     <d3>1.35</d3>
133     ...
134     <d24>0.23</d24>
135   </bestfit>
```

136 The `<param>` tag then contains the uncertainties and correlations in the form

```
137   <param>
138     <uncertainty axis="d1" side="left">-0.18</uncertainty>
139     <uncertainty axis="d1" side="right">+0.21</uncertainty>
140     <uncertainty axis="d2" side="left">-0.21</uncertainty>
141     <uncertainty axis="d2" side="right">+0.23</uncertainty>
142     ...
143     <uncertainty axis="d24" side="left">-0.88</uncertainty>
144     <uncertainty axis="d24" side="right">+1.03</uncertainty>
145
146     <correlation entry="d1d2">0.12</correlation>
147     <correlation entry="d1d3">0.16</correlation>
148     <correlation entry="d1d4">0.08</correlation>
149     ...
150     <correlation entry="d23d24">0</correlation>
151   </param>
152 </expmu>
```

153 This will also work for `type="n"`.

---

<sup>2</sup>The `<experiment>`, `<source>`, `<sqrts>`, etc. tags are omitted for brevity.

## Likelihood calculation

The statistic procedure used in `Lilith` was described in details in [1]. The main quantity given as an output is the  $-2 \log L$  which is computed according to the four different types of experimental data: 1D interval, 1D full, 2D contour, 2D full. Except for the full profile likelihoods, the  $-2 \log L$  values are computed using the ordinary Gaussian distribution approximation. Since we have found that this assumption does not describe very well data in many cases, therefore we have added the variable Gaussian and generalised Poisson distributions. We have also extended the code to include the multi-dimensional data. In this section we present in details how the  $-2 \log L$  quantities are computed according to the two distribution approximations. For the old implementation of the ordinary Gaussian distribution in `Lilith` we refer the reader to [1]. In the code, computations of  $-2 \log L$  are implemented in `computelikelihood.py`.

### The variable Gaussian distribution

As shown in [4], variable Gaussian distribution is one of good approximations to deal with asymmetric uncertainties. We apply the “Variable Gaussian (2)” in Section 3.6 of [4]. In the 1D interval case, the likelihood is given by

$$-2 \log L(\mu) = \frac{(\mu - \hat{\mu})^2}{\sigma^+ \sigma^- + (\sigma^+ - \sigma^-)(\mu - \hat{\mu})}, \quad (1)$$

where  $\hat{\mu}$  denotes the best-fit signal strength, and  $\sigma^-$  and  $\sigma^+$  are the left and right uncertainties at 68% CL, respectively. Note that  $\hat{\mu}, \sigma^-, \sigma^+$  are taken directly from experimental papers or fitted if they are not given explicitly. If not stated otherwise, these notations are used for the entire section. The ordinary Gaussian distribution is obtained with  $\sigma^+ = \sigma^-$ . The likelihood using variable Gaussian however has a singularity point at

$$\mu = \hat{\mu} - \frac{\sigma^+ \sigma^-}{\sigma^+ - \sigma^-}. \quad (2)$$

This may happens if the values of reduced couplings may be too large and unphysical. In the case of  $n$  dimension data ( $n > 1$ ), we use the  $n \times n$  correlation matrix given by the experimental collaboration, if it is available, together with the best fit points and the left and right uncertainties at 68% CL. Especially when data are given in terms of two dimensional contour plots, we can use also variable Gaussian to fit for the correlation and the best fit point and their uncertainties at 68 % CL, if they are not given explicitly by the experimental collaboration. For the  $n$  dimensional signal strength vector  $\boldsymbol{\mu} = (\mu_1, \dots, \mu_n)$ , the likelihood reads

$$-2 \log L(\boldsymbol{\mu}) = (\boldsymbol{\mu} - \hat{\boldsymbol{\mu}})^T C^{-1} (\boldsymbol{\mu} - \hat{\boldsymbol{\mu}}), \quad (3)$$

where the best fit point  $\hat{\boldsymbol{\mu}} = (\hat{\mu}_1, \dots, \hat{\mu}_n)$  and the covariance matrix is constructed from the correlation matrix  $\rho$  as

$$C = \boldsymbol{\Sigma}(\boldsymbol{\mu}) \cdot \rho \cdot \boldsymbol{\Sigma}(\boldsymbol{\mu}), \quad \boldsymbol{\Sigma}(\boldsymbol{\mu}) = \text{diag}(\Sigma_1, \dots, \Sigma_n) \quad (4)$$

with

$$\Sigma_i = \sqrt{\sigma_i^+ \sigma_i^- + (\sigma_i^+ - \sigma_i^-)(\mu_i - \hat{\mu}_i)}, \quad i = 1, \dots, n. \quad (5)$$

Here the  $\sigma_i^-$  and  $\sigma_i^+$  are the left and right uncertainties at 68% CL of the  $i$ th combination of production and decay channel, respectively. For the multi-dimensional data in the ordinary

188 Gaussian distribution, the relation between covariance matrix and the correlation matrix  
189 becomes

$$C = \frac{1}{4}[\boldsymbol{\sigma}^+ + \boldsymbol{\sigma}^-] \cdot \rho \cdot [\boldsymbol{\sigma}^+ + \boldsymbol{\sigma}^-], \quad (6)$$

190 where  $\boldsymbol{\sigma}^+ = \text{diag}(\sigma_1^+, \dots, \sigma_n^+)$  and  $\boldsymbol{\sigma}^- = \text{diag}(\sigma_1^-, \dots, \sigma_n^-)$ .

## 191 The generalised Poisson distribution

192 We apply the generalised Poisson distribution for one and two dimensional data. For the  
193 one dimensional data, the likelihood is implemented according to “Generalised Poisson”  
194 of [4],

$$\log L(\mu) = -\nu\gamma(\mu - \hat{\mu}) + \nu \log [1 + \gamma(\mu - \hat{\mu})], \quad (7)$$

195 where  $\gamma$  and  $\nu$  are solved numerically from the following equations

$$\frac{1 - \gamma\sigma^-}{1 + \gamma\sigma^+} = e^{-\gamma(\sigma^+ + \sigma^-)}, \quad \nu = \frac{1}{2(\gamma\sigma^+ - \log(1 + \gamma\sigma^+))}. \quad (8)$$

196 For the two dimensional data, we use the conditioning bivariate Poisson distribution de-  
197 scribed in [5], that has no restriction on the sign and magnitude of the correlation  $\rho$ .  
198 The joint distribution is a product of a marginal and a conditional distribution. The deci-  
199 sion of which channel belongs to the marginal or the conditional distribution is based on  
200 the validation plots. To illustrate our formulae, we assume that the data of the channel  
201  $X$  follows the marginal distribution while data of the channel  $Y$  belongs to the condi-  
202 tional distribution. The joint log-likelihood is the the sum of the marginal and conditional  
203 log-likelihoods

$$\log L(\mu_X, \mu_Y) = \log L(\mu_X) + \log L(\mu_Y | \mu_X), \quad (9)$$

204 where the marginal likelihood for the channel  $X$  is given by

$$\log L(\mu_X) = -\nu_X\gamma_X(\mu_X - \hat{\mu}_X) + \nu_X \log [1 + \gamma_X(\mu_X - \hat{\mu}_X)], \quad (10)$$

205 and the conditional likelihood for the channel  $Y$  given the channel  $X$

$$\log L(\mu_Y | \mu_X) = f(\mu_X, \mu_Y) - f(\hat{\mu}_X, \hat{\mu}_Y) + \nu_Y \log \frac{f(\mu_X, \mu_Y)}{f(\hat{\mu}_X, \hat{\mu}_Y)}. \quad (11)$$

206 Here the function  $f$  reads

$$f(a, b) = -\nu_Y\gamma_Y \left( b - \hat{\mu}_Y + \frac{1}{\gamma_Y} \right) \exp \left[ \nu_X\alpha - (e^\alpha - 1) \nu_X\gamma_X \left( a - \hat{\mu}_X + \frac{1}{\gamma_X} \right) \right], \quad (12)$$

207 where  $\alpha$  is solved numerically from the correlation expression

$$\rho = \frac{\nu_X\nu_Y(e^\alpha - 1)}{\sqrt{\nu_X\nu_Y \left[ 1 + \nu_Y \left( e^{\nu_X(e^\alpha - 1)} - 1 \right) \right]}}, \quad (13)$$

208 and the  $\gamma_x, \nu_X$  and  $\gamma_Y, \nu_Y$  are solutions of the Eq. 8 for the  $X$  and  $Y$  channels, respectively.

## 209 New production channels

210 In this section, the implementation of new production channels is described. They are  
 211 Higgs production in association with a single top quark  $tH$ ,  $ZH$  production via gluon-  
 212 gluon fusion  $ggZH$ , and Higgs production in association with two bottom quarks  $bbH$ .

213 The  $tH$  production includes two contributions:  $t$ -channel  $tHq$  production and  $tHW$   
 214 production. The  $s$ -channel  $tHq$  cross section is much smaller, hence not included. Inter-  
 215 ference effects between these channels are also neglected. At  $\sqrt{s} = 13$  TeV, the  $tHq$  cross  
 216 section is dominant, about 80% of the  $tH$  cross section. In order to compare with data,  
 217 e.g. ATLAS results [6], a combination of  $tHq$ ,  $tHW$ , and  $ttH$  channels named *top* signal  
 218 is defined. For relating the *top* and  $tH$  signal strengths to the signal strength of the fun-  
 219 damental production modes, the efficiencies of the fundamental channels are calculated as  
 220  $\sigma_X^{\text{SM}}/(\sum_X \sigma_X^{\text{SM}})$  where the  $ttH$  and  $tHq$  cross sections are provided in [7] while the  $tHW$   
 221 cross section is calculated at LO using MadGraph [8] with  $\mu_F = \mu_R = (m_t + m_W + m_H)/2$   
 222 and the NNPDF30\_lo\_as\_0130 PDF set [9]. It is noted that the definition of NLO cross  
 223 section for the  $tHW$  channel is not straightforward because of the interferences with the  
 224  $ttH$  channel, see [10] for a discussion on this issue.

225 For the  $ZH$  production mode, the original implementation in version 1 includes only  
 226 the  $q\bar{q} \rightarrow ZH$  channel ( $qqZH$ ). However, the loop-induced gluon-gluon fusion is not  
 227 so small, about 14% of the total  $ZH$  cross section at  $\sqrt{s} = 13$  TeV, hence should be  
 228 taken into account. Indeed, both ATLAS and CMS have been always including the  $ggZH$   
 229 contribution in their fits. From version 2, the  $ZH$  signal is the combination of  $qqZH$   
 230 and  $ggZH$  production modes. The efficiencies are calculated as above using the SM cross  
 231 section values given in [7]. The definition of  $VH$  ( $ZH$  and  $WH$ ) and  $VVH$  ( $ZH$ ,  $WH$   
 232 and  $VBF$ ) follow straightforwardly.

233 For the sake of completeness and to prepare for the future data, the  $bbH$  production  
 234 mode has been added. The implementation is straightforward, similar to the  $ttH$  case.

235 Finally, since Lilith accepts reduced couplings as user input, the relations between the  
 236 fundamental signal strengths (called scaling factors in [1]) and the reduced couplings must  
 237 be implemented. These relations read, following the notation of [1],

$$C_{bbH}^2 = C_b^2, \quad C_{qqZH}^2 = C_Z^2, \quad (14)$$

$$C_{ggZH}^2 = a_t C_t^2 + a_b C_b^2 + a_Z C_Z^2 + a_{tb} C_t C_b + a_{tZ} C_t C_Z + a_{bZ} C_b C_Z, \quad (15)$$

$$C_{tHq}^2 = e_t C_t^2 + e_W C_W^2 + e_{tW} C_t C_W, \quad (16)$$

$$C_{tHW}^2 = f_t C_t^2 + f_W C_W^2 + f_{tW} C_t C_W, \quad (17)$$

238 where the coefficients  $a_i$ ,  $e_i$ , and  $f_i$  are provided in Table 1 and Table 2. It is noted that  
 239 these values are calculated at  $m_H = 125$  GeV. For the case  $\sqrt{s} = 7$  TeV, the values at  
 8 TeV are used since the differences are negligible in the current approximations.

$\sqrt{s}$ [TeV]	$a_t$	$a_b$	$a_Z$	$a_{tb}$	$a_{tZ}$	$a_{bZ}$
8	0.372	0.0004	2.302	0.003	-1.663	-0.013
13	0.456	0.0004	2.455	0.003	-1.902	-0.011

Table 1:  $a_i$  coefficients for the  $ggZH$  signal strength. Taken from [7].

$\sqrt{s}$ TeV	$e_t$	$e_W$	$e_{tW}$	$f_t$	$f_W$	$f_{tW}$
8	2.984	3.886	-5.870	2.426	1.818	-3.244
13	2.633	3.578	-5.211	2.909	2.310	-4.220

Table 2:  $e_i$  ( $f_i$ ) coefficients for the  $tHq$  ( $tHW$ ) signal strengths. Taken from [7].



## ATLAS and CMS results included in the database update

### ATLAS Run 2 results for $36 \text{ fb}^{-1}$

The ATLAS Run 2 results included in this release are summarised in Table 3 and explained in more detail below.

mode	$\gamma\gamma$	$ZZ^*$	$WW^*$	$\tau\tau$	$b\bar{b}$	inv.
ggH	[6]	[11]	[12]	[13]	–	–
VBF	[6]	[11]	[12]	[13]	[14]	–
WH			–	–	[15]	–
ZH	[6]	[11]	–	–	[15]	[16]
ttH	[6, 17]	[11, 17]	[17]	[17]	[17, 18]	–

Table 3: Overview of ATLAS Run 2 results included in this release.

**$H \rightarrow \gamma\gamma$  (HIGG-2016-21):** The ATLAS analysis [6] provides in Fig. 12 signal strengths for  $H \rightarrow \gamma\gamma$  separated into ggH, VBF, VH and “top” (ttH+tH) production modes. No correlations are given for the signal strengths, but we can use instead the correlations for the stage-0 simplified template cross sections (STXS) provided in Fig. 40a of the ATLAS paper, which should be a close enough match. It turns out, however, that the  $\mu$  values rounded to one decimal do not allow to reproduce very well the ATLAS coupling fits for  $(C_V, C_F)$  or  $(C_\gamma, C_g)$ . We have therefore extracted the best-fit points and uncertainties from the 1D profile likelihoods, which are provided as Auxiliary Figures 23a–d on the analysis webpage, as  $\mu(\text{ggH}, \gamma\gamma) \simeq 0.81^{+0.19}_{-0.18}$ ,  $\mu(\text{VBF}, \gamma\gamma) \simeq 2.04^{+0.61}_{-0.53}$ ,  $\mu(\text{VH}, \gamma\gamma) \simeq 0.66^{+0.89}_{-0.80}$  and  $\mu(\text{ttH}, \gamma\gamma) \simeq 0.54^{+0.64}_{-0.55}$  (using a Poisson likelihood). These numbers are consistent with the rounded values in Fig. 12 of [6], but using more digits improves the coupling fits as shown in Fig. 1.

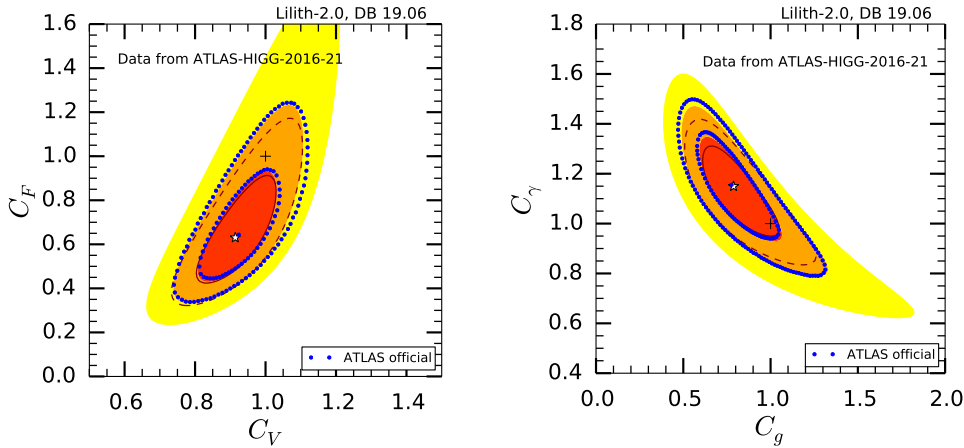


Figure 1: Fit of  $C_F$  vs.  $C_V$  (left) and  $C_\gamma$  vs.  $C_g$  (right) for data from the ATLAS  $H \rightarrow \gamma\gamma$  analysis [6]. The red, orange and yellow filled areas show the 68%, 95% and 99.7% CL regions obtained with Lilith using best-fit values and uncertainties for the signal strengths as extracted from Aux. Figs. 23a–d of the ATLAS analysis together with the  $4 \times 4$  correlation matrix for the stage-0 STXS. This can be compared to the 68%, 95% CL contours obtained using the rounded values from Fig. 12 of [3] (solid and dashed dark red lines) and to the official 68% and 95% CL contours from ATLAS (blue dots).

**$H \rightarrow ZZ^* \rightarrow 4l$  (HIGG-2016-22):** A similar issue as discussed for  $H \rightarrow \gamma\gamma$  above arises for  $H \rightarrow ZZ^*$ . In order to reasonably reproduce the  $C_F$  vs.  $C_V$  fit of ATLAS (Fig. 8b

of [11]), we fit the 1D profile likelihoods for  $\mu(\text{ggH}, ZZ^*)$  and  $\mu(\text{VBF}, ZZ^*)$  shown in Aux. Figs. 7a and 7b of [11] as Poisson distributions. This gives  $\mu(\text{ggH}, ZZ^*) \simeq 1.12^{+0.25}_{-0.22}$  and  $\mu(\text{VBF}, ZZ^*) \simeq 3.88^{+1.75}_{-1.46}$ , which we implement as a bivariate Poisson distribution with correlation  $\rho = -0.41$  (from Aux. Fig. 4c of [11]). For the VH and ttH production modes, lacking more information, we convert the given 95% CL limits into  $\mu(\text{VH}, ZZ^*) = 0 \pm 1.89$  and  $\mu(\text{ttH}, ZZ^*) = 0 \pm 3.83$  using a 2-sided Gaussian (the same for 1-sided limits give a less good result when comparing to the ATLAS  $C_F$  vs.  $C_V$  fit). The validation is shown in Fig. 2. Note that this is a case where the variable Gaussian approximation performs less well than the Poisson likelihood.

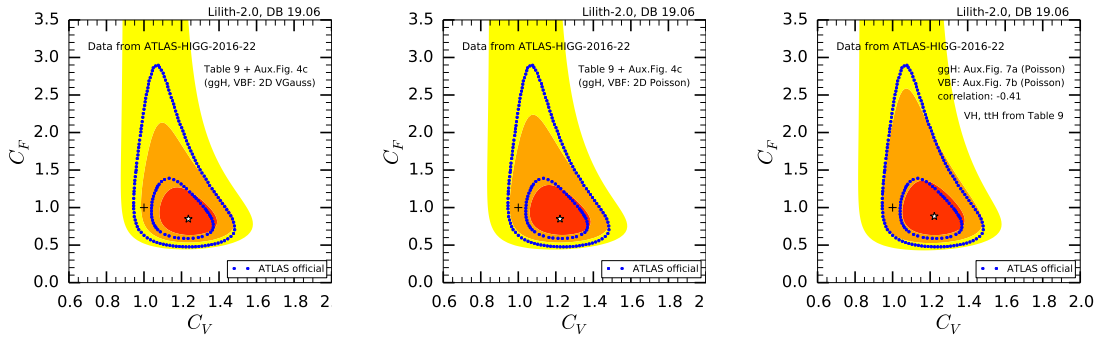


Figure 2: Fit of  $C_F$  vs.  $C_V$  for data from the ATLAS  $H \rightarrow ZZ^*$  analysis, using  $\mu(\text{ggH}, ZZ^*)$  and  $\mu(\text{VBF}, ZZ^*)$  as fitted from Aux. Figs. 7a and 7b of [11]; the ggH vs. VBF likelihood is then approximated as a bivariate Poissonian with correlation  $-0.41$  (see text for more details). The 68%, 95% and 99.7% CL regions obtained with Lilith are shown as red, orange and yellow areas, and compared to the 68% and 95% CL contours from ATLAS (in blue).

**$H \rightarrow WW^* \rightarrow 2l2\nu$  (HIGG-2016-07):** Ref. [12] focusses on the measurement of the inclusive ggH and VBF Higgs production cross sections in the  $H \rightarrow WW^* \rightarrow e\nu\mu\nu$  channel. The paper quotes on page 13 signal strengths of  $\mu(\text{ggH}, WW) = 1.10^{+0.21}_{-0.20}$  and  $\mu(\text{VBF}, WW) = 0.62^{+0.36}_{-0.35}$ . We implemented these as a 2D result with a correlation of  $\rho = -0.08$  using the variable Gaussian approximation; the correlation was fitted from the  $\sigma \times \text{BR}$  plot, Fig. 9, of [12]. As no other validation material is available, we show in Fig. 3 (left) our reconstruction of the experimental likelihood in the  $\mu(\text{ggH}, WW)$  vs.  $\mu(\text{VBF}, WW)$  plane, comparing to the rescaled contours of Fig. 9 of the ATLAS paper.

**$H \rightarrow \tau\tau$  (HIGG-2017-07):** This ATLAS cross section measurement in the  $H \rightarrow \tau\tau$  channel [13] provides as Aux. Fig. 5 the 68% and 95% CL contours in the  $\mu(\text{ggH}, \tau\tau)$  vs.  $\mu(\text{VBF}, \tau\tau)$  plane. A fit of a bivariate variable Gaussian to the 95% CL contour in this plot gives  $\mu(\text{ggH}, \tau\tau) \simeq 1.0^{+0.72}_{-0.59}$  and  $\mu(\text{VBF}, WW) = 1.20^{+0.62}_{-0.56}$  with  $\rho = -0.45$ , which are the values implemented in the database. As for  $H \rightarrow WW$  above, no coupling fits are available which could be used for validation. We therefore show in Fig. 3 (right) our reconstruction of the experimental likelihood in the  $\mu(\text{ggH}, \tau\tau)$  vs.  $\mu(\text{VBF}, \tau\tau)$  plane. Note that a fit to the 68% CL contour of ATLAS gives a less good result.

**$H \rightarrow b\bar{b}$  (HIGG-2016-29 and HIGG-2016-30):** For the  $H \rightarrow b\bar{b}$  decay mode, ATLAS gives  $\mu(\text{ZH}, b\bar{b}) = 1.12^{+0.50}_{-0.45}$ ,  $\mu(\text{WH}, b\bar{b}) = 1.35^{+0.68}_{-0.59}$  [14] and  $\mu(\text{VBF}, b\bar{b}) = 3.0^{+1.7}_{-1.6}$  [14]. No correlation data is available, so we implemented each of these as a 1D result; a Poisson likelihood is assumed per default but can easily be changed to a variable Gaussian if the user wishes to do so.

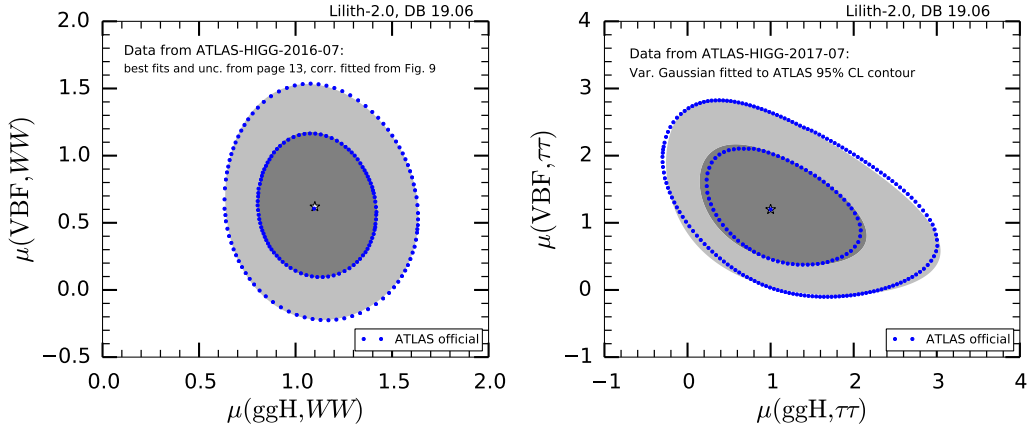


Figure 3: Reconstruction of the experimental likelihood as 2D variable Gaussian on the left for the  $H \rightarrow WW$  channel from [12], on the right for the  $H \rightarrow \tau\tau$  channel from [13]. The 68% and 95% CL regions obtained with *Lilith* are shown in dark and light gray, respectively, and compared to the 68% and 95% CL contours from ATLAS (in blue).

291

292  **$t\bar{t}H$  production (HIGG-2017-02):** The ATLAS paper [17], reporting evidence for  
 293  $t\bar{t}H$  production, provides in Fig. 16 the signal strength results broken down into  $H \rightarrow \gamma\gamma$ ,  
 294  $VV (= ZZ^* + WW^*)$ ,  $\tau\tau$  and  $b\bar{b}$  decay modes from a combined analysis of all  $t\bar{t}H$  searches.  
 295 Correlations are not given explicitly but can be estimated from Figs. 17a and 17b in [17]  
 296 as  $\rho(b\bar{b}, VV) \simeq 0.04$  for the correlation between the  $H \rightarrow b\bar{b}$  and  $H \rightarrow VV$  decay modes  
 297 and  $\rho(\tau\tau, VV) \simeq -0.35$  for that between the  $H \rightarrow \tau\tau$  and  $H \rightarrow VV$  decay modes. In  
 298 Fig. 4, we compare the  $C_F$  vs.  $C_V$  fit from the implementation in *Lilith* to the official  
 299 one from [17].

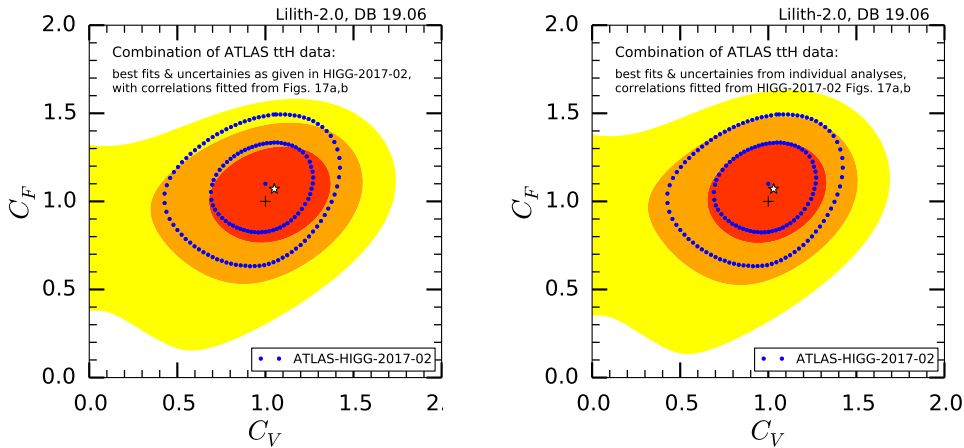


Figure 4: Fit of  $C_F$  vs.  $C_V$  from a combination of the ATLAS  $t\bar{t}H$  measurements, .... The 68%, 95% and 99.7% CL regions obtained with *Lilith* are shown as red, orange and yellow areas, and compared to the 68%, 95% CL contours from ATLAS (in blue).

300 A few comments are in order here. First, the measurement of  $\mu(t\bar{t}H, \gamma\gamma)$  actually comes  
 301 from [6] (HIGG-2016-21, see above) and is also included in the HIGG-2016-21 XML file;  
 302 to avoid overlap when using both the HIGG-2016-21 and HIGG-2017-02 datasets, we pro-  
 303 vide a 3D XML file for the latter which includes only the  $VV$ ,  $\tau\tau$  and  $b\bar{b}$ , but not the  $\gamma\gamma$ ,  
 304 decay modes. Second, the individual measurement [18] gives  $\mu(t\bar{t}H, b\bar{b})$  to two decimals

( $0.84^{+0.64}_{-0.61}$ ) instead just one ( $0.8 \pm 0.6$ ) in [17]. Since this makes a visible difference in Fig. 4, improving the quality of the fit, we use the more precise numbers from [18]. Third, for  $\mu(\text{t}\bar{\text{t}}\text{H}, VV)$  the contribution from  $H \rightarrow WW^*$  should dominate, but the concrete weights of the  $ZZ^*$  and  $WW^*$  decay modes are not given in [17]. This is not a problem as long as  $C_Z = C_W \equiv C_V$ , but one should not use the HIGG-2017-02 XML file for any other case.

**$H \rightarrow \text{invisible}$  (HIGG-2016-28):** Results from the search for invisibly decaying Higgs bosons produced in association with a  $Z$  boson are presented in [16]. A 95% CL upper limit of  $\text{BR}(H \rightarrow \text{inv.}) < 0.67$  is set for  $m_H = 125$  GeV assuming the SM  $ZH$  production cross section. In the Lilith database, we use a likelihood grid as function  $\text{BR}(H \rightarrow \text{inv.})$  extracted from Aux. Fig. 1c on the analysis' webpage.

### CMS Run 2 results for $36 \text{ fb}^{-1}$

The CMS Run 2 results included in this release are summarised in Table 4 and explained in more detail below.

mode	$\gamma\gamma$	$ZZ^*$	$WW^*$	$\tau\tau$	$b\bar{b}$	$\mu\mu$	inv.
ggH	[3]	[3]	[3]	[3]	[3]	[3]	[19]
VBF	[3]	[3]	[3]	[3]	–	[3]	[19]
WH	[3]	[3]	[3]	[20]	[3]	–	[19]
ZH	[3]	[3]	[3]	[20]	[3]	–	[19]
t $\bar{\text{t}}$ H	[3]	[3]	[3]	[3]	[3]	–	–

Table 4: Overview of CMS Run 2 results included in this release. Note that we use the full  $24 \times 24$  correlation matrix for the signal strengths for each production and decay mode combination provided in [3].

**Combined measurements (HIG-17-031):** CMS presented in [3] a combination of the individual measurements for the  $H \rightarrow \gamma\gamma$  [21],  $ZZ$  [22],  $WW$  [23],  $\tau\tau$  [24],  $b\bar{b}$  [25, 26] and  $\mu\mu$  [27] decay modes as well as the  $t\bar{t}H$  analyses [28–30]. We use the best fit values and uncertainties for the signal strengths for each production and decay mode combination presented in Table 3 of [3] together with the  $24 \times 24$  correlation matrix provided as “Additional Figure 1” on the analysis webpage. As shown in Figs. 5 and 6, this allows to reproduce well the coupling fits of the CMS paper.

**$VH, H \rightarrow \tau\tau$  (HIG-18-007):** The above data from [3] is supplemented by the results for the  $\tau\tau$  decay mode from the  $WH$  and  $ZH$  targeted analysis [20]. These are implemented in the form of 1D intervals for  $\mu(ZH, H \rightarrow \tau\tau)$  and  $\mu(WH, H \rightarrow \tau\tau)$  taken from Fig. 6 of [20].

**$H \rightarrow \text{invisible}$  (HIG-17-023):** In [19], CMS performed a search for invisible decays of a Higgs boson produced through vector boson fusion. We use the profile likelihood ratios for the qqH-tag, Z(l $\bar{l}$ )H-, V(qq')H- and ggH-tag categories extracted from their Fig. 8b together with the relative contributions from the different Higgs production mechanisms given in Table 6 of that paper. This assumes that the relative signal contributions stay roughly the same as for SM production cross sections. For validation, we reproduce in Fig. 7 the  $C_\gamma$  vs.  $C_\gamma$  fit of [3], where the branching ratios of invisible and undetected decays

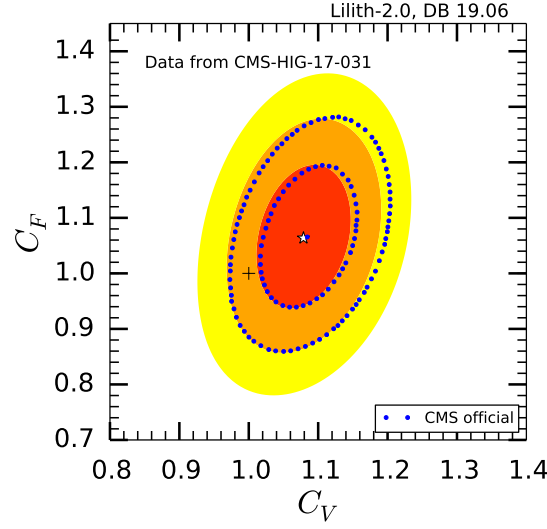


Figure 5: Fit of  $C_F$  vs.  $C_V$  using best-fit values and uncertainties for the signal strengths for each production (ggH, VBF, WH, ZH, ttH) and decay ( $\gamma\gamma$ ,  $ZZ$ ,  $WW$ ,  $\tau\tau$ ,  $b\bar{b}$ ,  $\mu\mu$ ) mode combination together with the  $24 \times 24$  correlation matrix from the CMS combination paper [3]. The  $1\sigma$ ,  $2\sigma$  and  $3\sigma$  regions obtained with *Lilith* are shown as red, orange and yellow areas, and compared to the  $1\sigma$  and  $2\sigma$  contours from CMS (blue dots).

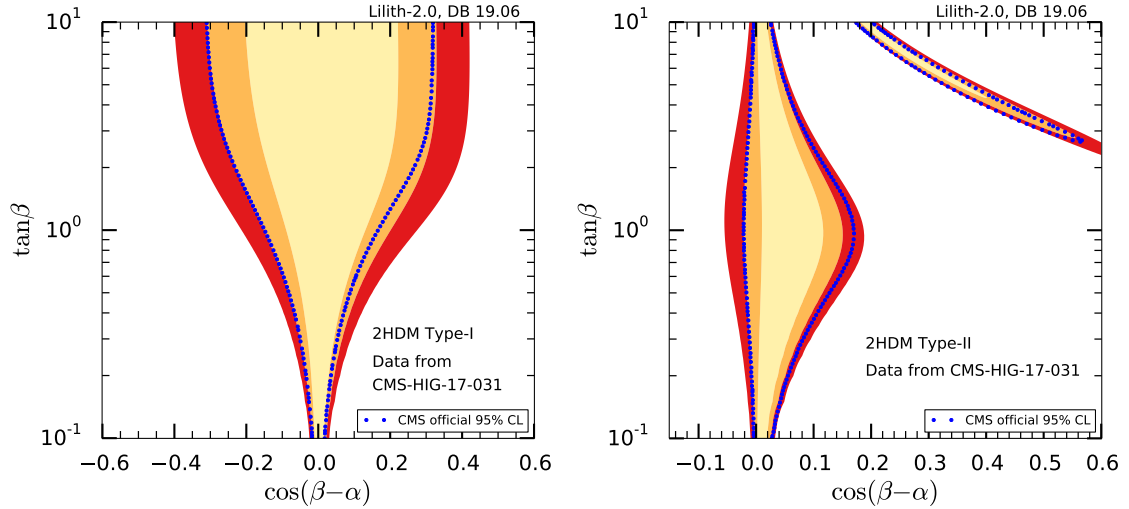


Figure 6: Fit of  $\tan\beta$  vs.  $\cos(\beta - \alpha)$  for the Two-Higgs-Doublet models of Type I (left) and Type II (right) using the data from the combined CMS measurement [3]. The beige, orange and red filled areas show the 68%, 95% and 99.7% CL regions obtained with *Lilith*, while the blue dots mark the 95% CL contours from CMS.

340 are treated as free parameters.<sup>3</sup>

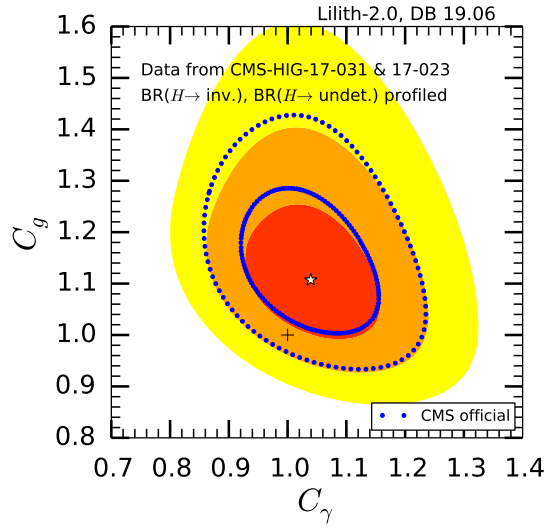


Figure 7: Fit of  $C_g$  vs.  $C_\gamma$  using the data from the combined CMS measurement [3] and the search for invisible decays of a Higgs boson [19]. The branching ratios of invisible and undetected decays are treated as free parameters in the fit. The  $1\sigma$ ,  $2\sigma$  and  $3\sigma$  regions obtained with Lilith are shown as red, orange and yellow areas, and compared to the  $1\sigma$  and  $2\sigma$  contours from CMS (in blue).

## 341 Status of Higgs coupling fits

342 In this section we give a brief overview of the current status of Higgs coupling fits. We  
 343 begin by showing in Fig. 8 fits of  $C_F$  vs.  $C_V$  (left panel) and  $C_g$  vs.  $C_\gamma$  (right panel) using

<sup>3</sup>The profiling in Fig. 7 was done with Minuit. Since Minuit does not allow conditional limits, in this case  $\text{BR}(H \rightarrow \text{inv.}) + \text{BR}(H \rightarrow \text{undet.}) < 1$ , we demanded that both  $\text{BR}(H \rightarrow \text{inv.})$  and  $\text{BR}(H \rightarrow \text{undet.})$  be less than 50%.

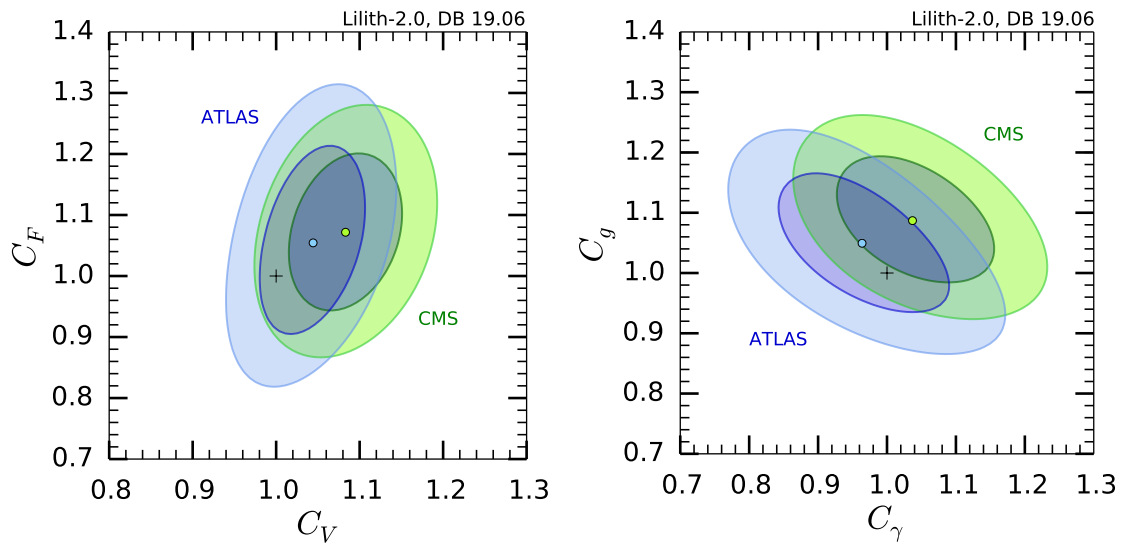


Figure 8: Fit of  $C_F$  vs.  $C_V$  (left) and  $C_g$  vs.  $C_\gamma$  (right) using the Run 2 dataset of the current database version, DB 19.06. The 68% and 95% CL regions for the combined ATLAS results are shown in blue, those for CMS in green.

either the ATLAS (in blue) or the CMS (in green) Run 2 results in the current Lilith database, DB 19.06. As can be seen, the two experiments agree at the level of about  $1\sigma$ .

The situation when combining the results from both experiments is shown in Fig. 9. Using the Run 2 (Run 2 + Run 1) results of DB 19.06, we find

$$C_F = 1.066^{+0.066}_{-0.065} (1.048^{+0.056}_{-0.055}), \quad C_V = 1.062 \pm 0.030 (1.059 \pm 0.025) \quad (18)$$

with a correlation of 0.31. This assumes that contributions from new particles to the loop-induced couplings to gluons and photons as well as invisible or undetected decays are absent. Taking instead  $C_g$  and  $C_\gamma$  as free parameters with  $C_F = C_V = 1$  (still assuming that invisible or undetected decays are absent), gives

$$C_g = 1.066^{+0.051}_{-0.050} (1.070^{+0.043}_{-0.043}), \quad C_\gamma = 0.999^{+0.055}_{-0.053} (1.004^{+0.048}_{-0.047}) \quad (19)$$

with correlation  $-0.52$  ( $-0.51$ ) from Run 2 (combining Run 2 and Run 1) results.

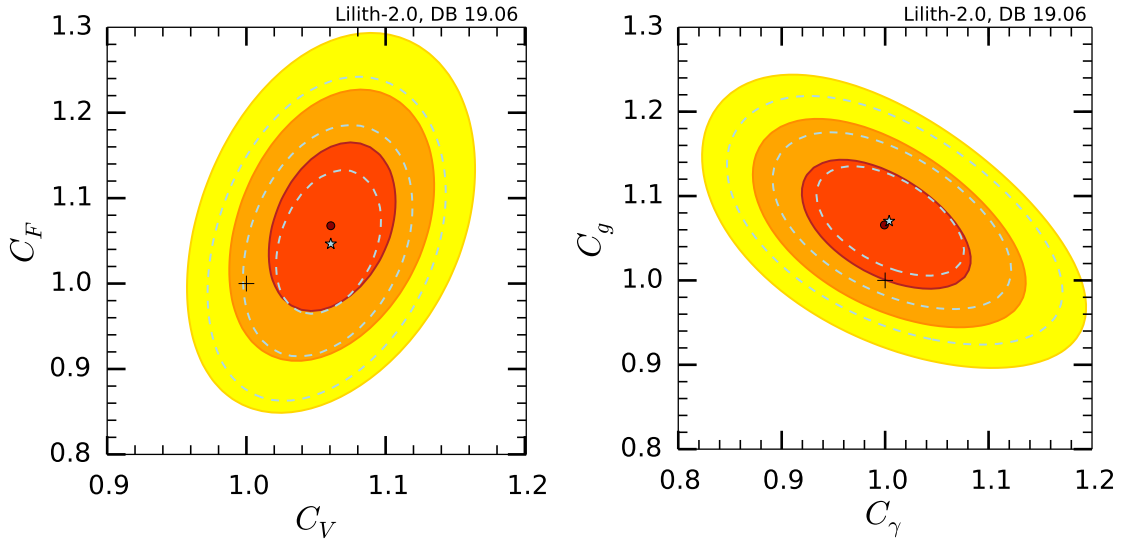


Figure 9: Fit of  $C_F$  vs.  $C_V$  (left) and  $C_g$  vs.  $C_\gamma$  (right) from a combination of the ATLAS and CMS Run 2 results in DB 19.06; the 68%, 95% and 99.7% CL regions are shown as red, orange and yellow areas, respectively. In addition, the light-blue, dashed contours indicate the 68%, 95% and 99.7% CL regions when combining the Run 2 and Run 1 data.

## Conclusion

must include a conclusion.

## Acknowledgements

S.K. thanks W. Adam, R. Schöfbeck, W. Waltenberger and N. Wardle for helpful discussions. This work was supported in part by the IN2P3 theory project “LHC-itools: methods and tools for the interpretation of the LHC Run 2 results for new physics”. D.T.N. thanks the LPSC Grenoble for hospitality and financial support for a research visit within the LHC-itools project. L.T.Q. thanks the ICISE ...



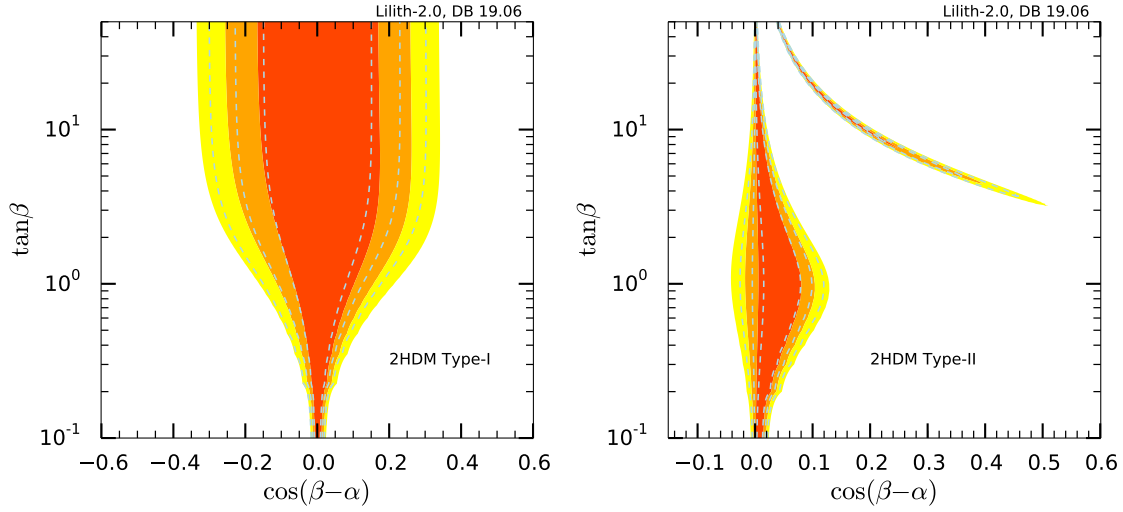


Figure 10: Fits of  $\cos(\beta - \alpha)$  versus  $\tan \beta$  for the 2HDM of Type I (left) and of Type II (right) from a combination of the ATLAS and CMS Run 2 results in DB 19.06. The red, orange and yellow areas are the 68.3%, 95.4% and 99.7% CL regions, respectively. In addition, the light-blue, dashed contours indicate the 68%, 95% and 99.7% CL regions when combining the Run 2 and Run 1 data. Loop contributions from charged Higgs bosons are neglected and decays into non-SM particles (such as  $h \rightarrow AA$ ) assumed to be absent.

## References

- [1] J. Bernon and B. Dumont, *Lilith: a tool for constraining new physics from Higgs measurements*, Eur. Phys. J. **C75**(9), 440 (2015), doi:10.1140/epjc/s10052-015-3645-9, 1502.04138.
- [2] G. Aad *et al.*, *Measurements of the Higgs boson production and decay rates and constraints on its couplings from a combined ATLAS and CMS analysis of the LHC  $pp$  collision data at  $\sqrt{s} = 7$  and 8 TeV*, JHEP **08**, 045 (2016), doi:10.1007/JHEP08(2016)045, 1606.02266.
- [3] A. M. Sirunyan *et al.*, *Combined measurements of Higgs boson couplings in proton–proton collisions at  $\sqrt{s} = 13$  TeV*, Eur. Phys. J. **C79**(5), 421 (2019), doi:10.1140/epjc/s10052-019-6909-y, <https://cms-results.web.cern.ch/cms-results/public-results/publications/HIG-17-031/>, 1809.10733.
- [4] R. Barlow, *Asymmetric statistical errors*, In *Statistical Problems in Particle Physics, Astrophysics and Cosmology (PHYSTAT 05): Proceedings, Oxford, UK, September 12-15, 2005*, pp. 56–59 (2004), physics/0406120.
- [5] P. Berkhout and E. Plug, *A bivariate Poisson count data model using conditional probabilities*, In *Statistica Neerlandica*, pp. 349–364 (2004).
- [6] M. Aaboud *et al.*, *Measurements of Higgs boson properties in the diphoton decay channel with  $36 \text{ fb}^{-1}$  of  $pp$  collision data at  $\sqrt{s} = 13$  TeV with the ATLAS detector*, Phys. Rev. **D98**, 052005 (2018), doi:10.1103/PhysRevD.98.052005, <https://atlas.web.cern.ch/Atlas/GROUPS/PHYSICS/PAPERS/HIGG-2016-21/>, 1802.04146.



- [7] D. de Florian *et al.*, *Handbook of LHC Higgs Cross Sections: 4. Deciphering the Nature of the Higgs Sector* (2016), doi:10.23731/CYRM-2017-002, <https://twiki.cern.ch/twiki/bin/view/LHCPhysics/LHCHXSWG2KAPPA>, 1610.07922.
- [8] J. Alwall, R. Frederix, S. Frixione, V. Hirschi, F. Maltoni, O. Mattelaer, H. S. Shao, T. Stelzer, P. Torrielli and M. Zaro, *The automated computation of tree-level and next-to-leading order differential cross sections, and their matching to parton shower simulations*, JHEP **07**, 079 (2014), doi:10.1007/JHEP07(2014)079, 1405.0301.
- [9] R. D. Ball *et al.*, *Parton distributions for the LHC Run II*, JHEP **04**, 040 (2015), doi:10.1007/JHEP04(2015)040, 1410.8849.
- [10] F. Demartin, B. Maier, F. Maltoni, K. Mawatari and M. Zaro,  *$tWH$  associated production at the LHC*, Eur. Phys. J. **C77**(1), 34 (2017), doi:10.1140/epjc/s10052-017-4601-7, 1607.05862.
- [11] M. Aaboud *et al.*, *Measurement of the Higgs boson coupling properties in the  $H \rightarrow ZZ^* \rightarrow 4\ell$  decay channel at  $\sqrt{s} = 13$  TeV with the ATLAS detector*, JHEP **03**, 095 (2018), doi:10.1007/JHEP03(2018)095, <https://atlas.web.cern.ch/Atlas/GROUPS/PHYSICS/PAPERS/HIGG-2016-22/>, 1712.02304.
- [12] M. Aaboud *et al.*, *Measurements of gluon-gluon fusion and vector-boson fusion Higgs boson production cross-sections in the  $H \rightarrow WW^* \rightarrow e\nu\mu\nu$  decay channel in  $pp$  collisions at  $\sqrt{s} = 13$  TeV with the ATLAS detector*, Phys. Lett. **B789**, 508 (2019), doi:10.1016/j.physletb.2018.11.064, <https://atlas.web.cern.ch/Atlas/GROUPS/PHYSICS/PAPERS/HIGG-2016-07/>, 1808.09054.
- [13] M. Aaboud *et al.*, *Cross-section measurements of the Higgs boson decaying into a pair of  $\tau$ -leptons in proton-proton collisions at  $\sqrt{s} = 13$  TeV with the ATLAS detector*, Phys. Rev. **D99**, 072001 (2019), doi:10.1103/PhysRevD.99.072001, <https://atlas.web.cern.ch/Atlas/GROUPS/PHYSICS/PAPERS/HIGG-2017-07/>, 1811.08856.
- [14] M. Aaboud *et al.*, *Search for Higgs bosons produced via vector-boson fusion and decaying into bottom quark pairs in  $\sqrt{s} = 13$  TeV  $pp$  collisions with the ATLAS detector*, Phys. Rev. **D98**(5), 052003 (2018), doi:10.1103/PhysRevD.98.052003, <https://atlas.web.cern.ch/Atlas/GROUPS/PHYSICS/PAPERS/HIGG-2016-30/>, 1807.08639.
- [15] M. Aaboud *et al.*, *Evidence for the  $H \rightarrow b\bar{b}$  decay with the ATLAS detector*, JHEP **12**, 024 (2017), doi:10.1007/JHEP12(2017)024, <https://atlas.web.cern.ch/Atlas/GROUPS/PHYSICS/PAPERS/HIGG-2016-29/>, 1708.03299.
- [16] M. Aaboud *et al.*, *Search for an invisibly decaying Higgs boson or dark matter candidates produced in association with a  $Z$  boson in  $pp$  collisions at  $\sqrt{s} = 13$  TeV with the ATLAS detector*, Phys. Lett. **B776**, 318 (2018), doi:10.1016/j.physletb.2017.11.049, <https://atlas.web.cern.ch/Atlas/GROUPS/PHYSICS/PAPERS/HIGG-2016-28/>, 1708.09624.
- [17] M. Aaboud *et al.*, *Evidence for the associated production of the Higgs boson and a top quark pair with the ATLAS detector*, Phys. Rev. **D97**(7), 072003 (2018), doi:10.1103/PhysRevD.97.072003, <https://atlas.web.cern.ch/Atlas/GROUPS/PHYSICS/PAPERS/HIGG-2017-02/>, 1712.08891.
- [18] M. Aaboud *et al.*, *Search for the standard model Higgs boson produced in association with top quarks and decaying into a  $b\bar{b}$  pair in  $pp$  collisions at*

- 425  $\sqrt{s} = 13$  TeV with the ATLAS detector, Phys. Rev. **D97**(7), 072016 (2018),  
 426 doi:10.1103/PhysRevD.97.072016, [https://atlas.web.cern.ch/Atlas/GROUPS/](https://atlas.web.cern.ch/Atlas/GROUPS/PHYSICS/PAPERS/HIGG-2017-03)  
 427 [PHYSICS/PAPERS/HIGG-2017-03](https://atlas.web.cern.ch/Atlas/GROUPS/PHYSICS/PAPERS/HIGG-2017-03), 1712.08895.
- 428 [19] A. M. Sirunyan *et al.*, Search for invisible decays of a Higgs boson pro-  
 429 duced through vector boson fusion in proton-proton collisions at  $\sqrt{s} = 13$  TeV  
 430 (2018), doi:10.1016/j.physletb.2019.04.025, [https://cms-results.web.cern.ch/](https://cms-results.web.cern.ch/cms-results/public-results/publications/HIG-17-023/)  
 431 [cms-results/public-results/publications/HIG-17-023/](https://cms-results.web.cern.ch/cms-results/public-results/publications/HIG-17-023/), 1809.05937.
- 432 [20] A. M. Sirunyan *et al.*, Search for the associated production of the Higgs boson and  
 433 a vector boson in proton-proton collisions at  $\sqrt{s} = 13$  TeV via Higgs boson decays  
 434 to  $\tau$  leptons, Submitted to: JHEP (2018), [https://cms-results.web.cern.ch/](https://cms-results.web.cern.ch/cms-results/public-results/publications/HIG-18-007/)  
 435 [cms-results/public-results/publications/HIG-18-007/](https://cms-results.web.cern.ch/cms-results/public-results/publications/HIG-18-007/), 1809.03590.
- 436 [21] A. M. Sirunyan *et al.*, Measurements of Higgs boson properties in the diphoton de-  
 437 cay channel in proton-proton collisions at  $\sqrt{s} = 13$  TeV, JHEP **11**, 185 (2018),  
 438 doi:10.1007/JHEP11(2018)185, 1804.02716.
- 439 [22] A. M. Sirunyan *et al.*, Measurements of properties of the Higgs boson decaying into  
 440 the four-lepton final state in  $pp$  collisions at  $\sqrt{s} = 13$  TeV, JHEP **11**, 047 (2017),  
 441 doi:10.1007/JHEP11(2017)047, 1706.09936.
- 442 [23] A. M. Sirunyan *et al.*, Measurements of properties of the Higgs boson decaying to  
 443 a  $W$  boson pair in  $pp$  collisions at  $\sqrt{s} = 13$  TeV, Phys. Lett. **B791**, 96 (2019),  
 444 doi:10.1016/j.physletb.2018.12.073, 1806.05246.
- 445 [24] A. M. Sirunyan *et al.*, Observation of the Higgs boson decay to a pair of  $\tau$  leptons with  
 446 the CMS detector, Phys. Lett. **B779**, 283 (2018), doi:10.1016/j.physletb.2018.02.004,  
 447 1708.00373.
- 448 [25] A. M. Sirunyan *et al.*, Evidence for the Higgs boson decay to a bottom quark–antiquark  
 449 pair, Phys. Lett. **B780**, 501 (2018), doi:10.1016/j.physletb.2018.02.050, 1709.07497.
- 450 [26] A. M. Sirunyan *et al.*, Inclusive search for a highly boosted Higgs boson decay-  
 451 ing to a bottom quark-antiquark pair, Phys. Rev. Lett. **120**(7), 071802 (2018),  
 452 doi:10.1103/PhysRevLett.120.071802, 1709.05543.
- 453 [27] A. M. Sirunyan *et al.*, Search for the Higgs boson decaying to two muons in  
 454 proton-proton collisions at  $\sqrt{s} = 13$  TeV, Phys. Rev. Lett. **122**(2), 021801 (2019),  
 455 doi:10.1103/PhysRevLett.122.021801, 1807.06325.
- 456 [28] A. M. Sirunyan *et al.*, Evidence for associated production of a Higgs boson with a top  
 457 quark pair in final states with electrons, muons, and hadronically decaying  $\tau$  leptons  
 458 at  $\sqrt{s} = 13$  TeV, JHEP **08**, 066 (2018), doi:10.1007/JHEP08(2018)066, 1803.05485.
- 459 [29] A. M. Sirunyan *et al.*, Search for  $t\bar{t}H$  production in the  $H \rightarrow b\bar{b}$  decay channel with  
 460 leptonic  $t\bar{t}$  decays in proton-proton collisions at  $\sqrt{s} = 13$  TeV, JHEP **03**, 026 (2019),  
 461 doi:10.1007/JHEP03(2019)026, 1804.03682.
- 462 [30] A. M. Sirunyan *et al.*, Search for  $t\bar{t}H$  production in the all-jet final state  
 463 in proton-proton collisions at  $\sqrt{s} = 13$  TeV, JHEP **06**, 101 (2018),  
 464 doi:10.1007/JHEP06(2018)101, 1803.06986.